Climatological Validation of TRMM TMI and PR Monthly Rain Products over Oklahoma

BRAD L. FISHER

Laboratory for Atmospheres and Science Systems and Applications, NASA Goddard Space Flight Center, Greenbelt, Maryland

(Manuscript received 6 February 2003, in final form 22 September 2003)

ABSTRACT

This paper reports the results from a regional validation study of monthly precipitation products generated from sensor measurements aboard the Tropical Rainfall Measuring Mission (TRMM) satellite. The study analyzed 4 yr of precipitation estimates (1998–2001) produced from data collected by the TRMM Microwave Imager (TMI) and the precipitation radar (PR) and compared them with corresponding estimates computed using 5-min rain accumulations from 66 rain gauges in the Oklahoma Mesonet. The applied methodology estimated bulk climate-scale sampling and retrieval errors and biases for the TMI and PR at two areal resolutions: $1^\circ \times 1^\circ$ and $2^\circ \times 5^\circ$. The approach taken in this study generated two gauge-inferred gridded estimates of monthly precipitation over the study period: 1) G_0, which was computed by performing a complete integration of the monthly gauge time series, and 2) G_S, which consisted of gauge-inferred rain rates subsampled to TRMM overpasses at a gridded resolution of $1^\circ \times 1^\circ$, with monthly precipitation estimates derived from the bulk statistics collected during each month of the study. The variable G_S depends on the areal swath of each sensor and so yields two sensor-dependent estimates of gauge-inferred precipitation (G_{TMI}, G_{PR}). The advantage of this approach is that it allows for the separation of retrieval and sampling errors, because the subsampled gauge estimates include the temporal sampling errors associated with the satellite sampling. The overall random sampling and retrieval errors for the PR exceeded the TMI errors for the study period, but the PR showed a greater reduction in the errors when the scale was increased to $2^\circ \times 5^\circ$. Annual coefficients of variation were also generally lower for the PR than the TMI at this scale. This result was consistent with PR retrieval biases, which were positive over all 4 yr, exceeding the TMI biases in every year of the study.

1. Introduction

Satellite meteorology is making important contributions to gaining a better understanding of the global water cycle and its effects on the large-scale dynamics of the atmospheric general circulation. Large-scale, time–area-averaged precipitation estimates from satellite observing platforms impart critical information about the mean climatological distribution and variability of precipitation on a global scale. In addition to having a larger sampling domain, satellites have a distinct advantage over ground sensors because they can gather information on precipitation processes over oceanic and mountainous regions, where in situ measurements of precipitation are extremely sparse or altogether nonexistent. Spaceborne sensors, however, collect radiance information remotely from cloud levels, and then use algorithms to obtain estimates of surface rain intensity based on the physical and statistical relations between radiance and precipitation. With continuing improvements in satellite remote sensing technology and algorithmic models, more attention is being placed on the quantitative accuracy of satellite rain retrievals.

The Tropical Rainfall Measuring Mission (TRMM) satellite was launched in November 1997 as a joint scientific initiative between the National Aeronautics and Space Administration (NASA) and the National Space Development Agency (NASDA) of Japan. The TRMM satellite collects precipitation information within a large sampling domain that extends from 40°N to 40°S. The two primary precipitation sensors onboard TRMM are the precipitation radar (PR) and the nine-channel TRMM Microwave Imager (TMI). The TMI collects passive radiance information at 10.7, 19.4, 21.3, 37.0, and 85.5 GHz and has a swath width of 758.8 km (Kummerow et al. 1998). All TMI channels are horizontally and vertically polarized, except for the 21.3-GHz channel, which is only vertically polarized. Each sensor collects instantaneous areal observations during satellite overpasses, with local satellite revisit times varying between once and twice daily. The PR instrument is a 128-element active phased-array system, operating at 13.8 GHz and covering a swath of 215 km. The PR is affected by attenuation caused by intervening precipitation and has a minimum detectable signal of about 17 dBZ.

Corresponding author address: Brad Fisher, Code 912.1, Bldg. 22, Room 166, NASA Goddard Space Flight Center, Greenbelt, MD 20771.
E-mail: fisher@radar.gsfc.nasa.gov

One of the major goals of TRMM is to produce quantitatively accurate mean monthly rain estimates from an earth-orbiting satellite with errors not exceeding 10%–15% of the true precipitation for a 5° × 5° grid space (Simpson et al. 1988). The original TRMM error model developed by Wilheit (1988) related errors in satellite precipitation estimates to three primary sources: retrieval, sampling, and random errors. Random errors relating to instrument noise and the statistical effects of thermal emission are small and do not contribute much to the overall error budget. Consequently, most of the subsequent work on the TRMM error budget has concentrated on errors associated with sampling and rain retrievals.

Retrieval errors are directly associated with the algorithm approximation to the physics used to generate estimates of instantaneous rain maps. Retrieval errors are associated with both a random and systematic component. It has been suggested that random retrieval errors should be small relative to the mean bias when averaged over 1 month of observations (~30 flush overpasses) (Wilheit 1988; Bell et al. 1990). The climatological averaging of the data then provides a way of probing the mean bias. Errors introduced by retrieval biases are of special interest to algorithm developers and other users of the data (Chang and Chiu 1999), because once the bias has been quantified, it can be removed, which can lead to improvements in the algorithms.

TRMM monthly estimates are derived from the mean rain rate obtained from the bulk statistics associated with a time series of discrete ''snapshots,'' which in the Tropics typically occur every 12–24 h. This noncontinuous sampling of precipitation by TRMM leads to sampling errors, in which the mean monthly rain rate inferred from the observational statistics does not fully represent the actual mean rain rate. Sampling errors are closely associated with the orbital characteristics of the satellite, which determine the sampling frequency, and the spatiotemporal structure of precipitation associated with diurnal, synoptic, seasonal, and interannual variability cycles. Although sampling errors tend to be randomly distributed, they are a significant part of the error budget, and subsequently may obstruct any quantitative determination of the mean retrieval bias associated climatological rain estimates.

The entanglement of sampling and retrieval errors in TRMM monthly rain estimates has been a much-studied problem, because a direct probing of any retrieval bias requires some knowledge of the errors due to sampling. Several researchers prior to the launch of TRMM presented detailed studies showing the statistical effects of discrete sampling. McConnell and North (1987), Shin and North (1988), North and Nakamoto (1989), and Bell et al. (1990) all concluded that TRMM sampling errors should average between 8% and 12% per month for 5° × 5° boxes. However, the primary focus of these studies was on the equatorial oceans. Moreover, several of the important sampling studies (Laughlin 1981; Bell et al. 1990; McConnell and North 1987) used rain statistics from the Global Atmospheric Research Program (GARP) Atlantic Tropical Experiment (GATE) to study the sampling problem. Oklahoma, the subject of this study, is located at the turning point of the satellite (i.e., changeover between ascending and descending orbits). The orbital characteristics of the satellite at this latitude and the rain climatology of Oklahoma are significantly different from what is typically observed over the equatorial oceans, such as the GATE area.

This study introduces an error model that empirically estimates sampling and retrieval errors for the TMI and PR adapted from earlier work by Bell et al. (2001). The methodology is fundamentally dependent on statistical rain estimates from gauges that have been subsampled at the satellite overpass times. These subsampled gauge rain estimates are assumed to incur an equivalent sampling error as the satellite sensor and provide an additional degree of freedom that is used to decouple the sampling and retrieval components of the total standard error. A dataset consisting of 66 high-resolution rain gauges from the Oklahoma Mesonet, and covering a 2° × 5° rectangular area in Oklahoma, were used to validate 4 yr of TRMM monthly estimates collected between 1998 and 2001. This area approximated a standard 5° × 5° TRMM box.

Section 2 of this paper provides descriptions of the datasets used in this study. Section 3 develops the formalism used for the error model. Section 4 describes the procedure that is used to subsample the gauge data at the satellite overpass times. This section also presents regression plots comparing subsampled gauge estimates with continuously integrated gauge estimates to further illustrate the effects of subsampling on rain estimation. Analysis and results are presented in sections 5 and 6, respectively. Section 7 is devoted to qualitatively discussing the systematic effects of TRMM sampling at latitudes near the satellite's turning point, and the possible existence of a climatological sampling bias for this regional location.

2. Data products

a. Satellite data products

TRMM satellite precipitation products are processed by the TRMM Science and Data Information System (TSDIS) and released to the general public through the Goddard Earth Sciences (GES) Distributed Active Archive Center (DAAC). Table 1 provides a summary of the TRMM rain products used in this study, which were all processed using TRMM version-5 rain algorithms. The reference numbers assigned to these different product levels correspond to the different stages of the processing. Detailed descriptions of TRMM products and the algorithms used to process the data can be found at the TRMM Project Web site (online at http://trmm.gsfc.nasa.gov/data_dir/ProductStatus.html).

TABLE 1. TRMM satellite products.

TRMM product	Sensor	Data resolution	Data description*
2A12	TMI	~6.9 km (85 GHz)	Instantaneous surface rain rates
2A25	PR	~4 km	Instantaneous surface rain rates
G2A12	TMI	0.5°	Instantaneous orbital track information for TMI, gridded instantaneous TMI rain rates
G2B31	Combined	0.1°	Instantaneous orbital track information for PR (Note: G2B31 rain rates are generated from both TMI and PR within intersection of TMI/PR orbital track.)
3A25	PR	0.5°	Gridded monthly rain estimates
3B31	TMI	1°	Gridded monthly rain estimates
3B42	Geo-IR	1°	Gridded daily IR rain estimates

* Only describes file information used in this study.

Figure 1 shows the 2° × 5° study area and its geographical partitioning into ten 1° × 1° cells. This 2° × 5° region covers an area from 34° to 36°N and 100° to 95°W, roughly the southern two-thirds of the state. The upper third of the state had to be excluded from the study because the PR swath did not collect data above 36°N.

Using TRMM level-3 products, monthly precipitation estimates were first obtained for the ten 1° × 1° boxes shown in Fig. 1. Gridded Orbital Level-2 products (G2A12 and G2B31) provided gridded instantaneous orbital track data at a resolution of 0.5° for the TMI and 0.1° for the PR. The orbital track information was used to subset the gauge time series to TRMM overpasses. Standard Level-2 products (2A12 and 2A25) were used to compile the corresponding rain-rate statistics for the TMI and PR at the characteristic resolution of each sensor.

b. Rain gauge data products

The Oklahoma Mesonet is operated and maintained by the Oklahoma Climate Survey (OCS). The mesonet consists of 118 automated weather stations that measure 10 meteorological variables, including precipitation. Each station reports by radio to a base receiving station every 15 min. The tipping-bucket gauges in the network accumulate rain in increments of 0.01 in. and produce a rain record every 5 min, even when no rain is measured (Brock et al. 1995). Rain-rate calibration curves are generated in the laboratory, and these corrections to the observed rain rates are applied in postanalysis. Rigorous criteria were used in the selection of sites in order to minimize systematic errors caused by wind, obstructions, and topography. Gauges were partitioned into 1° × 1° cells as shown Fig. 1. Table 2 provides a listing of the number of gauges used to compute the areal means of each cell.

Gauge rain rates were interpolated to 1-min values with a cubic-spline algorithm. This interval was chosen so that the gauge time stamp could be matched with the TRMM overpasses. Interpolated rain rates were automatically bias adjusted for each observed rain event. Bias adjustments were generally between 1% and 5%, which ensured that over- and underestimations of precipitation were not introduced through the interpolating algorithm.

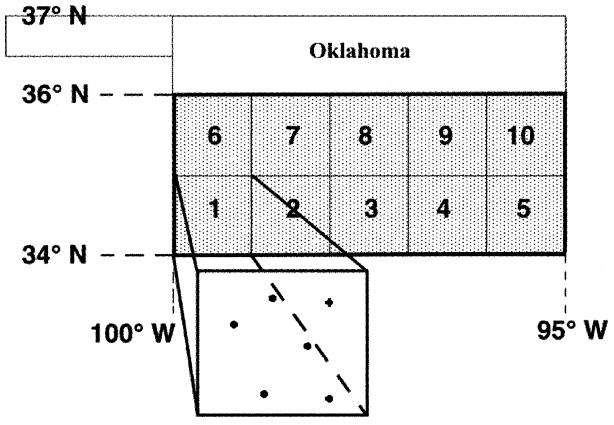

FIG. 1. Illustration showing the geographical partitioning of the 2° × 5° study area in Oklahoma into ten 1° × 1° cells. Each cell number corresponds to a row number in Table 2.

3. Error model

This section provides a description of the error model used in this study. The error corresponding to a given

TABLE 2. Number of gauges per 1° × 1° cell.

Cell No.	No. gauges
1	5
2	6
3	8
4	9
5	7
6	5
7	6
8	7
9	5
10	8

monthly areal rain estimate R_0 is defined as the magnitude of its deviation from the true mean areal precipitation R_T:

$$\varepsilon = R_0 - R_T. \quad (1)$$

In estimating the total error associated with a large number of such estimates, it is more practical to define the error in terms of a statistical variance. In the error model described by Wilheit (1988), the total error is related to two primary sources of variance, retrieval ($\sigma^2_{\text{err},R}$), and sampling ($\sigma^2_{\text{err},S}$) as

$$\langle (R_0' - R_T')^2 \rangle = \sigma^2_{\text{err},R} + \sigma^2_{\text{err},S}. \quad (2)$$

In (2) it is assumed that $\sigma^2_{\text{err},R}$ and $\sigma^2_{\text{err},S}$ are uncorrelated and that R_T is obtained from a perfect rain sensor that incurs no error itself. These assumptions are justified because retrieval errors are incurred in conjunction with satellite overpasses, whereas sampling errors are incurred when the satellite is not overhead. The primed quantities are used to indicate the deviation from the ensemble mean, that is, $R_0' = R_0 - \langle R_0 \rangle$.

In most practical situations, R_T is replaced by an independent estimate of surface precipitation, derived from measurements obtained from surface instruments. In this study, a gridded network of rain gauges were used to physically validate satellite rain estimates. Treating R_T as an observed quantity rather than an ideal quantity contributes an additional error variance in (2) related to the validation sensor (Bell and Kundu 2003). If R_T is replaced with G_0, then

$$\langle (R_0' - G_0')^2 \rangle = \sigma^2_{\text{err},R} + \sigma^2_{\text{err},S} + \sigma^2_{\text{err},G}. \quad (3)$$

In (3), G_0 provides an estimate of mean precipitation representing the same areal region and temporal period as R_0, and incurs an error variance $\sigma^2_{\text{err},G}$, which is assumed to be uncorrelated with the other two error terms in (3).

The use of G_0 as an estimate of R_T is based on the implicit assumption that gauge errors are at least one order of magnitude smaller than the satellite errors shown in (3). Three different sources of error contribute to the variance $\sigma^2_{\text{err},G}$:

$$\sigma^2_{\text{err},G} = \sigma^2_{\text{rand}} + \sigma^2_{\text{SS}} + \sigma^2_{\text{syst}}, \quad (4)$$

where σ^2_{rand}, σ^2_{SS}, and σ^2_{sys} correspond to random instrument error, spatial sampling error, and systematic gauge error, respectively. Random instrument errors associated with tipping-bucket measurements vary nonlinearly with rain rate but are typically only about $\pm 0.5\%$ per 0.254 mm. Spatial sampling errors are incurred when point gauge estimates are used to estimate areal precipitation. Gauge spatial sampling errors will be qualitatively addressed later in this section. Systematic gauge errors due to wind, frozen precipitation, topography, obstructions (such as trees and buildings), and mechanical and maintenance-related issues can be significant in some cases and so generally cannot be entirely ignored (Habib et al. 2001). The Oklahoma Mesonet gauges are closely monitored using telemetry, and so systematic errors will be treated as negligible in this study (Brock et al. 1995).

The mesonet gauges used in this study are sampling continuously and record precipitation at a high temporal resolution. Hence, the gauges are assumed to contain no temporal sampling errors from discrete sampling. The precipitation estimate of an individual gauge g_i can then be expressed in terms of the integral

$$g_i = \frac{1}{T} \int_0^T r_G(t)\, dt, \quad (5)$$

where $r_G(t)$ represents the complete recorded time series of precipitation for the gauge and T represents the duration of the validation period. The mean areal precipitation, denoted as G_0 in (3), is obtained by averaging the gauge estimates g_i within a gridded box containing N_G gauges:

$$G_0 = \frac{1}{N} \sum_{i=1}^{N_g} g_i. \quad (6)$$

As noted above, the individual gauge estimates contain negligible temporal sampling error, but G_0 contains spatial sampling errors associated with using an ensemble of point rain estimates to represent the mean precipitation over a larger gridded area.

The aim of this study is to determine $\sigma^2_{\text{err},R}$ and $\sigma^2_{\text{err},S}$ for the TMI and PR. However, the two estimates of precipitation, G_0 and R_0, by themselves do not provide enough information to decouple $\sigma^2_{\text{err},R}$ and $\sigma^2_{\text{err},S}$, which are associated with R_0. This problem was treated theoretically by Bell et al. (2001) by considering TRMM rain estimates, together with estimates from a geosynchronous, TRMM-like satellite that sampled the same region continuously. It was assumed that the additional satellite estimates incurred retrieval errors equivalent to those in the TRMM data. This rain estimate provided an additional degree of freedom that facilitated a decoupling of the random sampling and retrieval errors. The current study takes a complementary approach, in which the additional rain estimate is obtained by subsampling a network of rain gauges to the satellite overpass times. Because the sampling error depends on the sensor's data coverage, the subsampling procedure must be applied independently to both the TMI and PR. It is assumed that the resulting subsampled gauge estimates contain the TRMM sampling error for the shaded region shown in Fig. 1. The random temporal sampling error is then inferred from the variance between continuously sampled and sensor-dependent, subsampled gauge estimates, G_0 and G_S, respectively, whereas the retrieval error is related to the variance between the satellite rain estimate R_0 and G_S, as follows:

$$\sigma^2_{\text{err},S} = \langle (G_S' - G_0')^2 \rangle \quad \text{and} \quad (7)$$

$$\sigma^2_{\text{err},R} = \langle (R_0' - G_S')^2 \rangle. \quad (8)$$

Note that in Bell et al. (2001), the additional satellite

estimate assumed that the two satellites incur the same retrieval error, whereas in this case the TRMM satellite and subsampled gauges are assumed to contain the same sampling error.

Equations (7) and (8) only characterize random sampling and retrieval errors associated with TRMM sensors. Because these errors can represent a substantial fraction of the monthly mean precipitation estimates (random sampling errors alone are expected to be about 10%), a further characterization of the TRMM error budget can be ascertained from computations of any relative climatological biases related to sampling and retrievals. The expressions for the biases can be derived in a manner analogous to (7) and (8):

$$b_S = \left\langle \frac{G_S - G_0}{G_0} \right\rangle \quad \text{and} \tag{9}$$

$$b_R = \left\langle \frac{R_0 - G_S}{G_0} \right\rangle. \tag{10}$$

Equations (9) and (10) express the sampling and retrieval biases relative to G_0. The main aim of computing these biases is to estimate what fraction of over- and underestimates is associated with TRMM sampling and retrievals. However, this analysis will also probe the existence of any real climatological bias that may prevail from one year to the next. In this study, the biases were averaged over the annual cycle in order to eliminate some of the short-term random errors incurred from month to month.

The error model that has been described in this section assumes that the gauge and satellite spatiotemporal observational reference frames are statistically equivalent. It is this assumption that allows for the temporal sampling error of the satellite to be inferred purely on the basis of continuous and subsampled gauge data, without any direct consideration of R_0. Gauges, however, only represent point measurements. Spatial sampling errors occur because no rain information exists in the large amount of space between the gauges used to compute G_0. In order to provide a good statistical indicator of areal precipitation, the gauge network should be designed to minimize the spatial sampling errors associated with spatially discontinuous precipitation estimates (Huff 1970; Rodriguez-Iturbe and Mejia 1974b; North and Nakamoto 1989; Barnston 1991; Hulme and New 1997). Previous studies show that controlling and optimizing the relative distribution and density of gauges in the network can effectively minimize the spatial sampling errors associated with gauge-inferred areal estimates (Rodriguez-Iturbe and Mejia 1974a; North and Nakamoto 1989; Morrissey et al. 1995).

In a study that intercompared gauge monthly rain observations with satellite-inferred rain estimates, Xie and Arkin (1995) considered it necessary to have at least five gauges in a 2.5 grid box in order to ensure 10% accuracy in the gauge mean estimates for the box. Krajewski et al. (2000) quantified error variances in the Global Precipitation Climatology Project (GPCP) global dataset at 14 reference sites in the United States. One requirement of this study was that each 2.5° grid box had to contain a minimum of 25 gauges, with each gauge remaining operational over the whole validation period. This fairly rigorous criterion was intended to minimize random and systematic errors in the validation dataset. The current study used 66 gauges distributed within the $2° \times 5°$ area, shown in Fig. 1, which gauge density easily satisfies the Krajewski et al. criteria. In another relevant study, Morrissey et al. (1995) used the Oklahoma Mesonet to test the sensitivity of a gauge network configuration on the error variance, building on earlier work of Rodriguez-Iturbe and Mejia (1974a). This study found that a homogenous distribution of gauges minimized the error as compared to the following other gauge configurations: homogeneous, random, clustered, and two linear networks. The gauge configuration of the Oklahoma Mesonet closely approximates a quasi-homogenous configuration. Consequently, this gauge network must be considered one of the best in the world for doing large-scale satellite validation.

4. Gauge data: Methodology and analysis

a. Formal procedure for estimating G_S for the TMI and PR

Monthly estimates of G_S were generated from the bulk statistics associated with the discrete time series of ''gauge snapshots'' collected during 1 month of TRMM overpasses. Those applied in this study took advantage of the high temporal sampling resolution of the gauges by subsampling the gauge time series during coincident satellite overpasses, using the orbital track information obtained from the gridded level-2 products described in Table 2 (G2A12 and G2B31). The TRMM satellite collects about 80 observations per month for each sensor over the study area in Oklahoma. Each observation, however, only results in partial coverage of the region shown in Fig. 1. Thus, in an average month, TRMM sensors sample the full $2° \times 5°$ study region about 30 times. In this study, coverage was determined at the $1° \times 1°$ scale.

Without any loss of generality, the procedure described in this section derives the gauge-inferred mean monthly precipitation for a $1° \times 1°$ cell for a single month. In this study, if the satellite sampled any part of the grid box, then all of the gauges in the box were included in the estimation of the mean precipitation for that box. For each gauge, a time-averaged rain rate was computed by centering a constant time window Δt_w on a given overpass time t_k:

$$\hat{R}_i^{(G)}(t_k) = \frac{1}{\Delta t_w} \sum_{t=t_k-\Delta t_w/2}^{t_k+\Delta t_w/2} R_i^{(G)}(t), \tag{11}$$

where the subscript i corresponds to the ith gauge inside

of a given cell at the kth overpass. A time interval of 61 min was used in this study, based on model predictions by Bell and Kundu (2003). They plotted the relative sampling error as a function of the averaging time for a 1° × 1° cell containing nine equispaced gauges. For this area and gauge configuration (assuming equal gauge spacing), it was found that an averaging time of about 1 h minimized the sampling error associated with a single TRMM overflight.

Using (11), an estimate of the mean monthly precipitation for the ith gauge is then computed as

$$\overline{R}_i^{(G)} = \frac{1}{N_0} \sum_{k=1}^{N_0} \hat{R}_i^{(G)}(t_k), \tag{12}$$

where N_0 represented the number of TRMM overpasses for the month. Note that, in general, N_0 varies by month and from cell to cell. The sensor-dependent gauge-inferred mean monthly precipitation was defined as

$$G_S = \frac{1}{N_g} \sum_{i=1}^{N_g} \overline{R}_i^{(G)}, \tag{13}$$

where N_g represented the number of gauges used in computing a monthly average rain rate for a particular 1° × 1° cell.

Using G_S, sampling and retrieval errors and biases were subsequently computed using (7), (8), (9), and (10) at both 1° × 1° and 2° × 5° scales. Extending G_S to the 2° × 5° areal region of interest shown in Fig. 1 simply involved averaging the results from the 10 cells covering the larger area. Additional averaging produced significant reductions in random errors. This analysis will be presented in sections 5 and 6. It should be noted that the sensor-dependent gauge estimate G_S described in this and the previous sections will be subscripted with the sensor used in its generation, for example, G_{TMI} and G_{PR}.

b. G_0 versus G_{TMI}, G_{PR}

The effects of discrete temporal sampling were first investigated by looking at linear regressions of G_0 and sensor-dependent gauge estimates. The six panels in Fig. 2 show the results of a regression analysis of G_0 versus G_{TMI} and G_{PR} using monthly gauge estimates from 4 yr (1998–2001) of data at resolutions of 1° × 1° and 2° × 5°. Scatterplots performed at 2° × 5° are shown at two different temporal resolutions: monthly and 4-yr monthly averaged. The corresponding correlation coefficients for each case are listed in Table 3. This table also includes correlation coefficients that relate satellite (R_0) and gauge estimates (G_0, G_{TMI}, G_{PR}). These correlations will be discussed in section 5a.

Figures 2a and 2b reveal a large sampling variance at the 1° × 1° scale, with a resulting regression line that is weighted toward higher values of G_{TMI} and G_{PR}. Although the gridded gauge estimates G_0, G_{TMI}, and G_{PR} remain correlated, the regressions show a distinct broadening of the variance due to the temporal sampling of the G_0 time series, along with a reduction in the correlations between G_0 and sensor-dependent subsampled gauge estimates. The higher TMI correlation coefficient is slightly higher than the coefficient computed for the PR, which is likely attributable to the larger area of coverage associated with the TMI swath. If both sensor swaths are assumed to be flush with the study area, more gauge estimates are used in the estimation of G_{TMI} and G_{PR}. Figures 2c–2f show similar results for regressions performed at 2° × 5°, computed at the two temporal resolutions described above. Both cases show improved correlations and reduced sampling variance, but the regression lines still shows some evidence for a conditional sampling bias associated with the higher precipitation amounts.

Figure 3 displays the probability distribution of gauge-inferred sampling errors for the TMI and PR based on all of the differences between monthly estimates of G_{TMI}, G_{PR}, and G_0 computed over the four study years at a resolution of 1° × 1°. The two distributions shown in Fig. 3 are approximately normal. The median, mean, and standard deviations for each distribution were −0.21, 0.12, and 1.91 mm day^{-1} for the TMI, and −0.32, 0.16, and 2.31 mm day^{-1} for the PR, respectively. The TMI and PR sampling error spectrums are nearly equal from a statistical standpoint. The second moment for the PR spectrum is slightly broader, and it will be shown in the next two sections that this broadening relates a broader spectrum of monthly rain rates, as characterized by probability density functions shown in section 5b, and a broader instantaneous rain-rate distribution, shown in section 6b.

5. Statistical analysis of Level-3 satellite products with gauges

a. Regression analysis of monthly satellite and gauge estimates

Figures 4a and 4b display a 4-yr time series of mean monthly rain estimates at the 2° × 5° resolution for 1) G_0, G_{TMI}, and TMI, and 2) G_0, G_{PR}, and PR, respectively. These plots can be compared with the scatterplots shown in Figs. 5 and 6, where TMI and PR satellite rain estimates are matched against corresponding gauge rain estimates at the following spatiotemporal resolutions: 1) 1° × 1° using monthly estimates, 2) 2° × 5° using monthly estimates, and 3) climatological 4-yr monthly estimates. The correlation coefficients corresponding to these regressions are shown in Table 3.

The correlation between gauge and satellite rain estimates improved markedly as the spatial and temporal averaging scale was increased. Figures 5a,b and 6a,b show the regression plots performed for the TMI and PR monthly estimates at the 1° × 1° scale against predictands G_0, G_{TMI}, and G_{PR}. At this resolution, significant random errors are evident between the satellite and gauge estimates. Clearly, there exists a strong bias be-

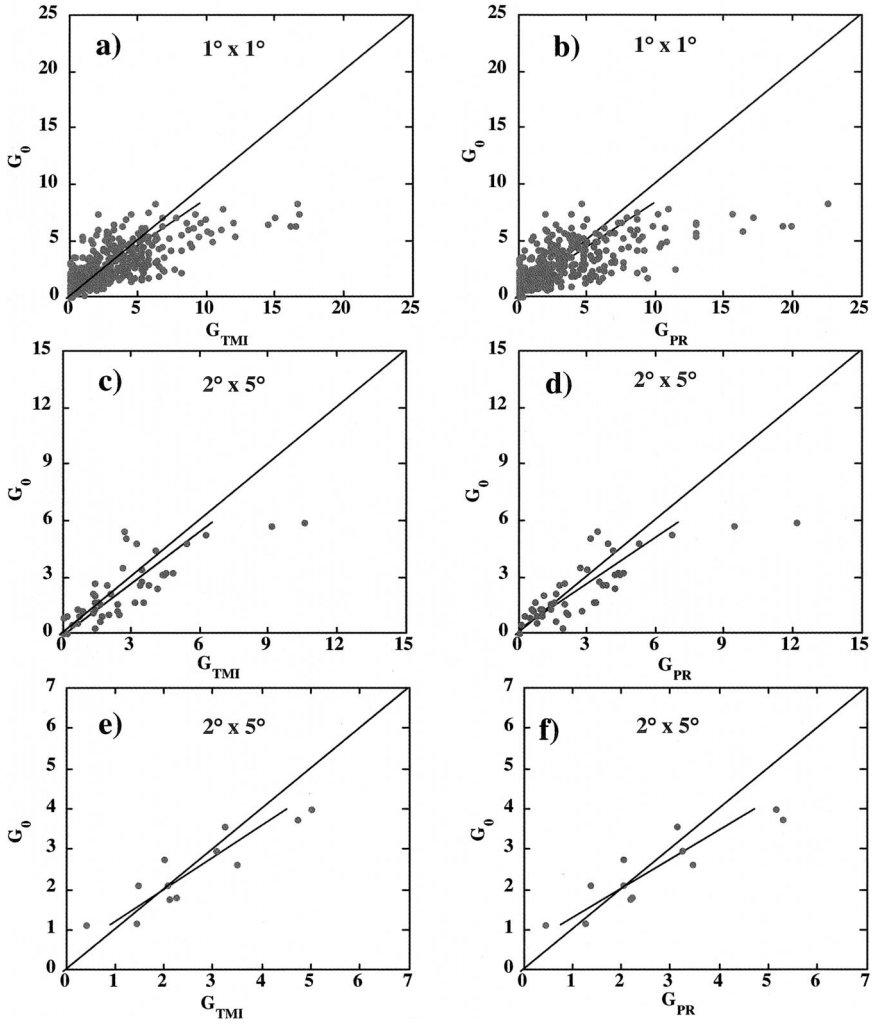

FIG. 2. Regressions of monthly rain estimates G_0 and subsampled gauge estimates (a) G_{TMI} and (b) G_{PR} at 1° × 1° resolution, using monthly estimates (480 points); (c) G_{TMI} and (d) G_{PR} at 2° × 5° resolution, using monthly estimates (48 points); and (e) G_{TMI} and (f) G_{PR} at 2° × 5° resolution using climatological 4-yr monthly estimates (12 points).

tween G_0 and both satellite sensors. The regression plots also show evidence of a bias between subsampled gauge estimates and the satellite estimates, as suggested by the weighting of the regression line. Correlations improve and random errors are reduced when the spatial scale is enlarged to 2° × 5°. However, TMI and PR regressions with both gauge precipitation parameters (G_0, G_{TMI}, and G_{PR}) still reveal the presence of a bias in regressions carried out at the larger scale. Examination of the slope in Fig. 5 shows that high rain amounts for the TMI tend to produce a positive satellite bias, whereas lower rain amounts tend to result in a negative satellite bias. The PR shows a strong positive bias for high rain amounts; however, for lower rain amounts the tendency to underestimate is not as consistent as in the case of the TMI. In fact, Fig. 6, showing monthly averages, suggests that there is a tendency for the PR to overestimate monthly rain amounts at both the high and low end.

TABLE 3. Correlation coefficients at grid resolutions of 1° × 1° and 2° × 5°. Independent predictor variables are listed in the rows, whereas the dependent variables are listed in the columns; G_S will represent either G_{TMI} or G_{PR}, depending on the sensor listed in each row.

	1° × 1° (all months)		2° × 5° (all months)		2° × 5° (4-yr monthly avg)	
Sensor	G_0	G_S	G_0	G_S	G_0	G_S
TMI	0.44	0.31	0.55	0.54	0.72	0.80
PR	0.46	0.27	0.65	0.55	0.85	0.78
G_{TMI}	0.74	1.0	0.80	1.0	0.90	1.0
G_{PR}	0.70	1.0	0.82	1.0	0.89	1.0

The results presented in this section for the TMI are consistent with Morrissey and Janowiak (1996). They

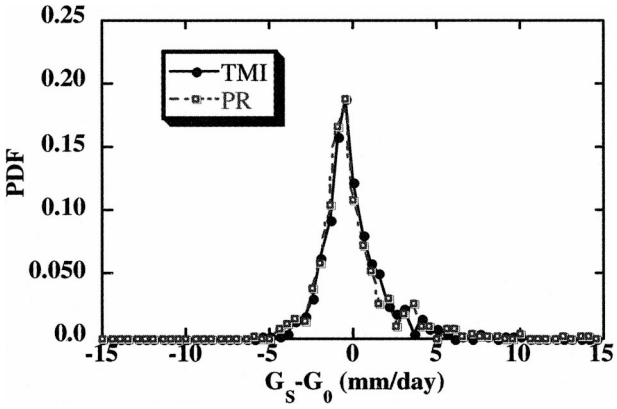

FIG. 3. Probability distribution of sampling errors for the TMI (solid) and PR (dashed) for all four study years (1998–2001). Data were binned at 0.5 mm day^{-1} intervals at a resolution of 1° × 1° (480 data points).

examined statistical regressions generated from climate-scale satellite and gauge rainfall estimations and related relative over- and underestimations of precipitation to the presence of a conditional sampling bias. This sampling bias was found to be dependent on the value of the estimate, and was closely associated with the slope of the regression line. Their analysis revealed a positive satellite bias for high precipitation events and a negative bias for low precipitation events. This sampling anomaly was attributed to the temporal sampling rate and its coupling to the autocorrelation structure of the precipitation processes. By estimating the autocorrelation structure of the rainfall, they were then able to apply a simple bias correction procedure.

b. Probability density functions for TMI, PR, 3B42, G_{TMI}, G_{PR}, and G_0

The effects of discrete sampling were further investigated by examining the probability density functions (PDFs) compiled from 4 yr (1998–2001) of monthly rain events at the 1° × 1° scale. Each distribution consisted of 480 points (10 cells × 12 months × 4 yr), binned at 0.5-mm intervals. Figure 7a displays PDFs for the TMI, G_{TMI}, and G_0, and similarly, Fig. 7b displays PDFs for the PR, G_{PR}, and G_0.

Each of the three panels shown in Fig. 7 are associated with two plots: a main and an inner plot. The main plot displays the probability density function ranging from 0 to 10 mm day^{-1}, whereas the inner plot extends the range out to 25 mm day^{-1}, with an expanded vertical axis to better show the fine structure in the tail of each distribution. Figures 7a and 7b show that most of the probability density is distributed in the 0–10 mm day^{-1} range. Although monthly rain events associated with the tail of the distribution represented a considerably smaller percentage of the cumulative probability, they played an important role in determining the total precipitation volume associated with each distribution.

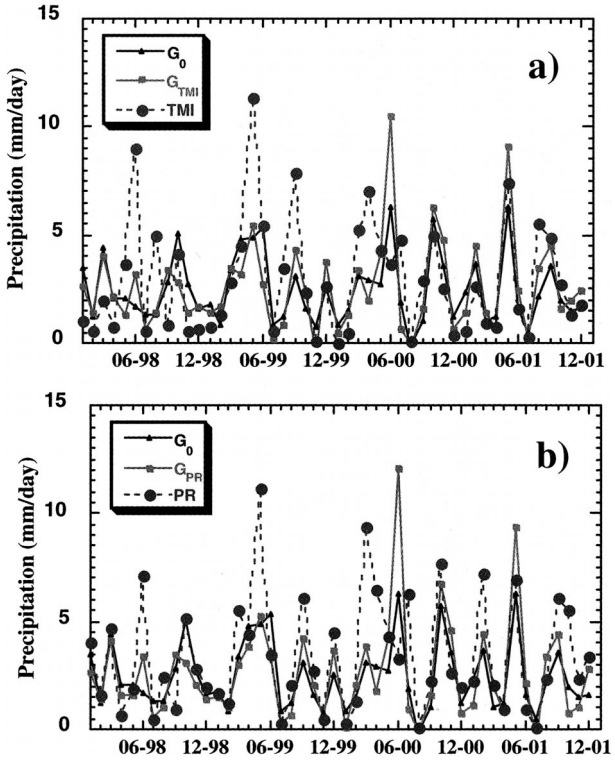

FIG. 4. Four-year time series (1998–2001) of monthly precipitation estimates for (a) G_0, G_{TMI}, and TMI, and (b) G_0, G_{PR}, and PR. Note that G_0 is independent of the two sensors and is the same in both plots.

The TMI, PR, and G_{TMI}, G_{PR} PDFs shown in Figs. 7a and 7b have a similar structure, with a maximum probability in the first rain bin (i.e., 0–0.5 mm day^{-1}), followed by an exponential decay in probability density. The effects of discrete temporal sampling can be clearly observed by comparing the PDFs for the TMI, G_{TMI}, and PR, G_{PR} curves with G_0 at the extreme ranges of each spectrum. The PDF for G_0 showed a relatively low probability of observing trace monthly precipitation (~8%), with 0 probability of observing gridded monthly rain totals that exceeded 8 mm day^{-1}. The PDF for G_{PR}, on the other hand, closely matched the PR spectrum in the first range bin (~26%), with an exponential tail that extended well beyond the observed threshold for G_0 (as shown in the inner plot). The PDF for the TMI and G_{TMI} were also closely matched, revealing a similar exponential distribution, but with a higher frequency of monthly estimates for the TMI in the first range bin (~31%). The higher fraction of zero/trace rain events observed by the TMI is, perhaps, due to the TMI sensor not observing weak rain systems with ice particle sizes and concentrations below its detectable levels (i.e., small ice-scattering cross section).

Huffman (1997) showed that random sampling errors were closely related to the shape of the probability distribution of precipitation, considered as a function of the rain rate. The observed differences shown in Figs.

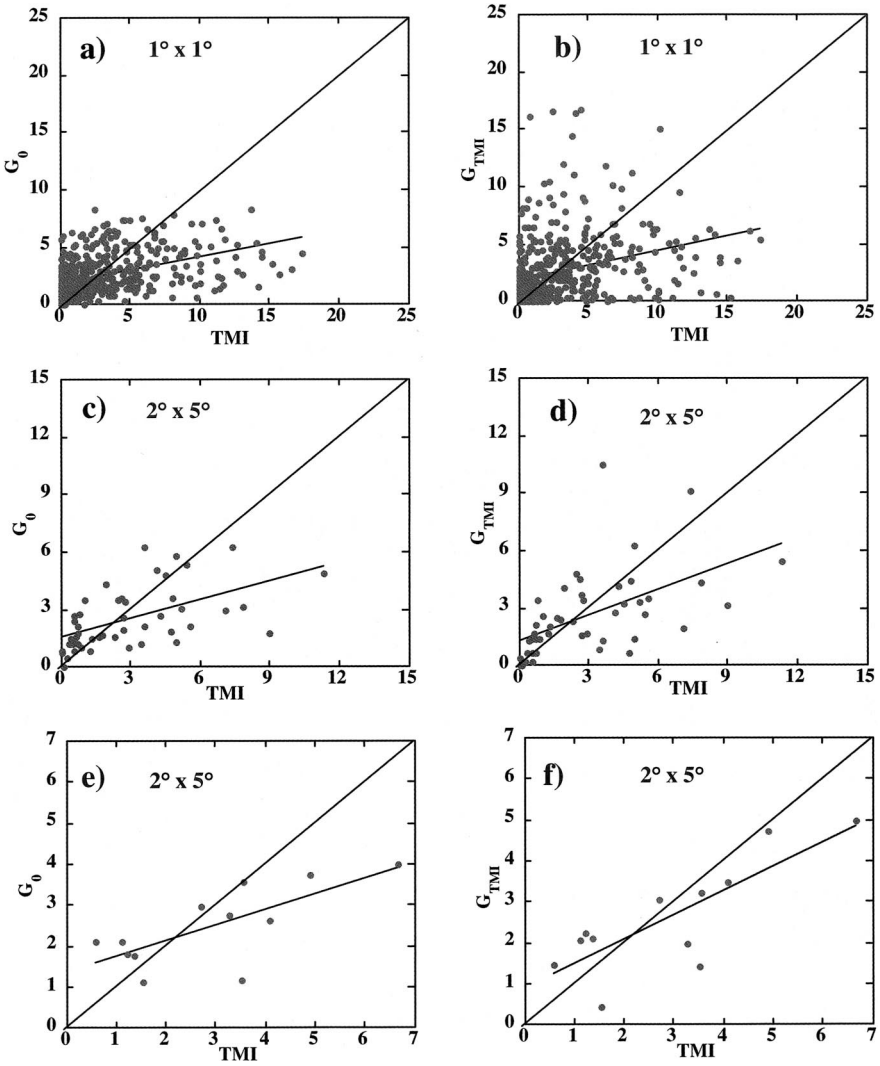

FIG. 5. Regressions of monthly rain estimates for TMI vs G_0 and G_{TMI} at different spatiotemporal resolutions (mm day^{-1}): (a) G_0 and (b) G_{TMI} at $1° \times 1°$ resolution, using monthly estimates (480 points); (c) G_0 and (d) G_{TMI} at $2° \times 5°$ resolution, using monthly estimates (48 points); and (e) G_0 and (f) G_{TMI} at $2° \times 5°$ resolution using 4-yr monthly means (12 points).

7a and 7b between the probability density functions computed for G_{TMI}, G_{PR}, and G_0 appear directly associated with the effects of discrete temporal sampling. Note that the sampling biases computed from (9) and (10) can be related to the mean differences between these two probability distributions, which exhibit a different probability structure. The PDF spectra at $2° \times 5°$ are not shown because the sample size was too small, but it is expected that, as the averaging domain is increased, the sampling errors will decrease and the PDF spectra for the TMI, PR, G_{TMI}, and G_{PR} will, in turn, show a tendency to converge on G_0.

The differences observed in the PDFs shown in Figs. 7a and 7b can be further related to the sampling frequency and the autocorrelation structure of precipitation at the $1° \times 1°$ scale by looking at the 3B42 TRMM rain product described in Table 1. This TRMM product estimates daily precipitation from eight samples a day (3-h sampling frequency). The 3-hourly rain estimates are computed using the Global Precipitation Index (GPI) adjustment to the TRMM combined rain product (2B31) based on coincident GPI and 2B31 data matchups for 1 month (Adler at al. 1994). Figure 7c displays a PDF profile of monthly precipitation estimates for the 3B42 for the same period of study. The 3B42 profile is more similar to the G_0 profile than it is to the TMI, G_{TMI}, or PR, G_{PR} profiles, which we ascribe to the additional sampling.

Laughlin (1981) estimated the autocorrelation time at the $1° \times 1°$ scale to be about 3.5 h, a value well matched with 3B42 sampling frequency at this spatial scale. It is, however, significantly less than the mean satellite

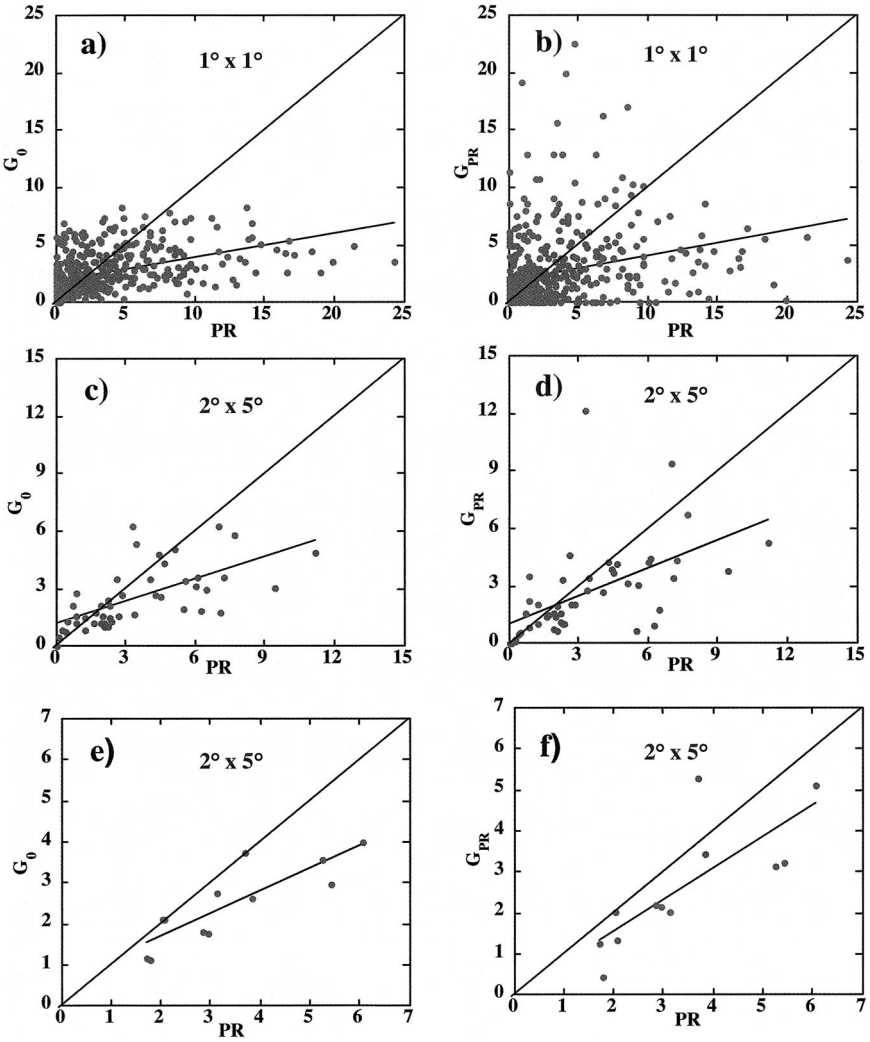

FIG. 6. Regressions of monthly rain estimates for PR vs G_0 and G_{PR} at different spatiotemporal resolutions (mm day^{-1}): (a) G_0 and (b) G_{PR} at 1° × 1° resolution, using monthly estimates (480 points); (c) G_0 and (d) G_{PR} at 2° × 5° resolution, using monthly estimates (48 points); and (e) G_0 and (f) G_{PR} at 2° × 5° resolution 4-yr monthly means (12 points).

revisit time for TRMM, which over Oklahoma is about 10.5 h. The 3B42 profile shown in Fig. 7c is also a good illustration of the central limit theorem, stating that the sample distribution will converge on the population as the number of independent samples increases. At the 2° × 5° scale, the autocorrelation time increases to about 8 h, a value more consistent with the TRMM mean revisit time over Oklahoma.

6. Results

a. TMI and PR error statistics: Annual means, standard errors, and biases

Error statistics were generated using the error model described in section 3 for the region shown in Fig. 1 over the 4-yr validation period. Shin and North (1988) and Shin et al. (1990) showed that the natural variance of rainfall in GATE data was inversely related to the size of the averaging area and was directly proportional to the sampling variance. One of the aims of this study was to empirically probe the effects of scale on TRMM error budget estimates by comparing standard errors and biases computed at 1° × 1° and 2° × 5°.

Table 4 reports the standard sampling and retrieval errors for each of the four study years using (7) and (8). Standard errors representing the entire study period were computed in two ways—by using all monthly estimates (48 points) and from 4-yr monthly averaged rain estimates (12 points). These overall results are presented in the last two columns of Table 4. The annual and overall means computed for each sensor for the 2° × 5° region studied are reported in Table 5. The means listed in this table are independent of the grid size. From the results presented in Tables 4 and 5, it is clear that

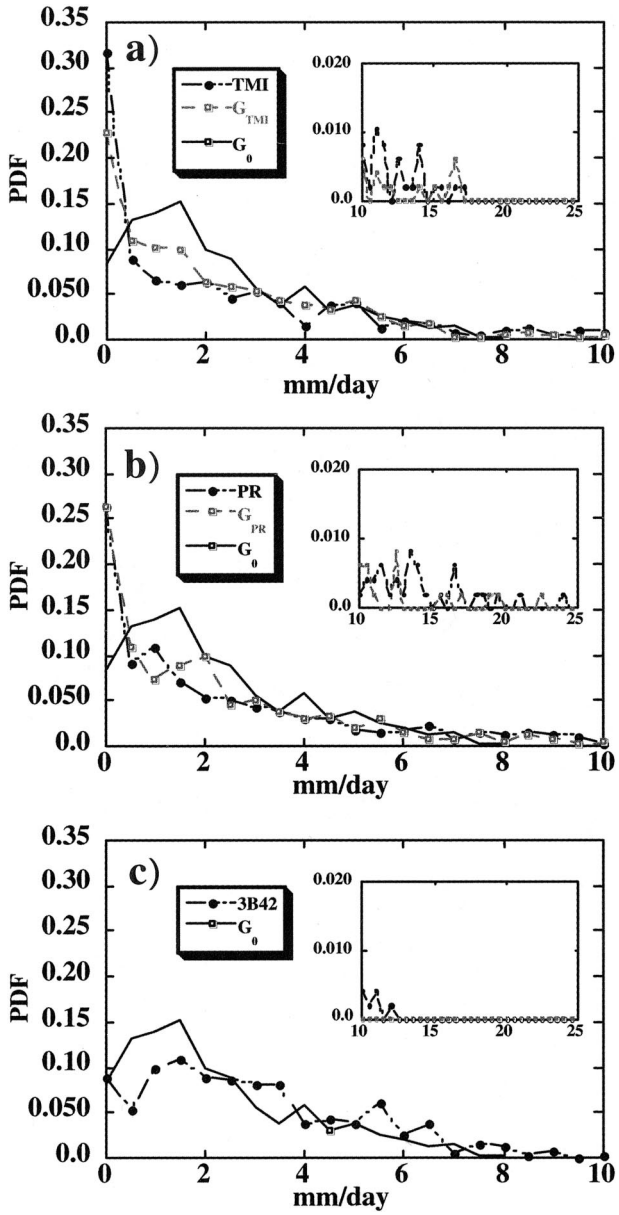

FIG. 7. Monthly probability density functions computed at 1° × 1° resolution for (a) TMI, G_{TMI}, and G_0; (b) PR, G_{PR}, and G_0; and (c) 3B42 (adjusted GPI) and G_0. The dynamic range on the larger outer plot extends to 10 mm day^{-1}. The smaller inner plot, with its adjusted scaling on the vertical axis, extends the horizontal range from 10 to 25 mm day^{-1}. The inner plot displays the fine structure in the tail of each distribution.

a significant reduction in errors was achieved through additional averaging. A further reduction of the standard errors was obtained through a monthly time averaging of the 4-yr data. TMI sampling and retrieval errors shown in Table 4 tended to be lower than the PR at the 1° × 1° scale. At 2° × 5°, however, the PR sampling and retrieval errors were reduced by a larger amount, resulting in lower standard errors than the TMI in 1998 and 1999. This result suggests that relative to the TMI, the higher-resolution PR footprint more than compensates for its narrower swath, because the precipitation measurements collected are averaged over a larger spatiotemporal domain.

Using the data values listed in Tables 4 and 5, sampling and retrieval coefficients of variation (CV) were computed for each sensor at 1° × 1° and 2° × 5°. These results are plotted in Figs. 8a and 8b, with CV expressed as the ratio of the standard error to the mean precipitation. The CV in Fig. 8 were computed relative to the respective annual means for each sensor. In Fig. 8a, the sampling errors of the two sensors differed only marginally from year to year at the 1° × 1° scale, with a 4-yr mean CV of about 0.65 for both sensors. However, at the larger 2° × 5° scale, the PR revealed a smaller CV in 1998, 1999, and 2001, with a 4-yr average of 0.34 as compared with 0.39 for the TMI. This result was unexpected based purely on sensor swath considerations and will be explored further in future research.

In extending the scale out to 2° × 5°, sampling errors, as measured by the mean CV, were reduced by 47% for the PR as compared with 40% for the TMI. Similar results were observed for retrievals, with errors reduced by 51% for the PR and 41% for the TMI. Sampling errors, in particular, were larger than expected based on prelaunch predictions. This result can be attributed to two main factors, one relating to the orbital characteristics of TRMM at high latitudes and the other to differences in the climatology over land. This issue will be discussed more in section 7.

Annually averaged satellite sampling and retrieval biases for the TMI and PR were computed using (9) and (10). These results shown plotted in Figs. 9a and 9b were based on 1-yr 2° × 5° averaging. As expected, the sampling biases were fairly well correlated for the two sensors. Both sensors observed negative biases during 1998 and 1999 and positive biases were observed for 2001. In 2000, biases for the TMI and PR biases had opposite signs, but their absolute difference was only marginal. An apparent sampling anomaly was observed in 2001 for the TMI, which resulted in a large sampling bias of $\sim 0.13 G_0$. The PR only revealed a bias of 5.5%. During the other three study years, the PR biases showed a slightly greater absolute magnitude. A closer examination of the data for year 2001 revealed a discrepancy between the two sensors in November, the only month for which the signs of the biases were opposite each other (TMI $>$ 0; PR $<$ 0). When this month was excluded, the annual sampling biases for the two sensors were $\sim 0.11 G_0$ for the TMI and $\sim 0.9 G_0$ for the PR. The year 2001 was the only year for which the sampling biases for either sensor exceeded $0.10 G_0$. It was also the only year for which G_{TMI} exceeded the TMI estimate and, hence, the only the year that produced a negative TMI retrieval bias. Summing the biases over all 4 yr produced an overall bias of about $-0.01 G_0$ and $-0.09 G_0$ for the TMI and PR, respectively.

As shown in Fig. 9b, PR retrieval biases exceeded

TABLE 4. Annual and 4-yr standard errors (sampling and retrieval) for the TMI and PR (mm day^{-1}).

Spatial grid	TRMM sensor	1998		1999		2000		2001		1998–2001 (all months)		1998–2001 (4-yr monthly avg)	
		σ_S	σ_R	σ_S	σ_R	σ_S	σ_R	σ_S	σ_R	σ_S	σ_R	σ_S	σ_R
1° × 1°	TMI	1.41	3.37	1.50	3.35	2.30	4.49	2.14	3.19	1.91	3.67	0.93	1.73
	PR	1.58	3.35	1.64	3.81	2.85	5.94	2.72	4.25	2.31	4.33	1.16	2.44
2° × 5°	TMI	0.93	2.43	1.12	2.04	1.40	2.94	0.96	1.07	1.17	2.29	0.61	1.04
	PR	0.85	1.48	0.83	1.61	1.77	3.70	1.17	1.84	1.28	2.35	0.72	0.94

the TMI in all four study years. Both sensors showed positive biases for 1998, 1999, and 2000, whereas in 2001 the TMI showed a negative bias of about $-0.09G_0$ as compared with $0.35G_0$ for the PR. In general, retrieval biases were within the range of 20%–60% of G_0. Over the tropical oceans the TMI rainfall retrievals have been shown to exceed the PR; however, Kummerow et al. show that the PR tends to exceed the TMI for land regions above 20°N (Kummerow et al. 2000; Serra and McPhaden 2003).

b. Instantaneous rain-rate profiles: TMI, PR, and G_0

Monthly precipitation accumulations are statistically coupled to rain retrievals obtained during instantaneous satellite overpasses. Figure 10 shows lognormal plots of instantaneous rain rate for the TMI, PR, and G_0 (1-min resolution). The gauge rain rates were compiled from all available data between 1998 and 2001 to approximate a climatological distribution. The anomalous spikes observed in the central part of the gauge distribution in Fig. 10 were introduced by the cubic spline transformation used to generate a time-continuous record of rain rates from a discrete time series of tips. Because of the large volume of data involved, TMI and PR distributions generated a representative sample consisting of 56 rain cases over Oklahoma. Standard Level-2 products were used (2A12 and 2A25) to pick a diverse grouping of rain cases from all four seasons that covered all 4 yr of the study. Gridded rain rates were not used in this analysis because the process of averaging eliminated important structural characteristics associated with the algorithms, moreover, gridded rain rates are only made available for the TMI.

The TMI rain-rate distribution shown in Fig. 10 appears structurally discrete and does not exceed a threshold of 50 mm h^{-1} (~17 dBR). Data collected over land are processed using only the brightness temperature information in the 85-GHz channels, limiting the retrieval to precipitation estimations based on scattering signals from ice hydrometeors (Spencer et al. 1989). The other TMI channels are not used because of difficulties in resolving the rain signal from the highly variable emissions coming from the land surface beneath the cloud column (Ferraro and Marks 1995). In general, the TMI land estimates surface precipitation by matching brightness temperature depressions from the TMI channels to a database of brightness temperature–rain-rate profiles generated by the Goddard Cumulus Ensemble Model (Tao and Simpson 1993; Kummerow et al. 2001). In

TABLE 5. Mean annual precipitation for TMI, G_{TMI}, PR, G_{PR}, and G_0.

	1998	1999	2000	2001	1998–2001
TMI	2.38	3.58	3.02	2.52	2.88
G_{TMI}	2.16	2.45	2.99	2.80	2.60
PR	2.81	3.63	3.82	3.33	3.40
G_{PR}	2.20	2.45	3.23	2.68	2.64
G_0	2.49	2.60	2.56	2.28	2.48

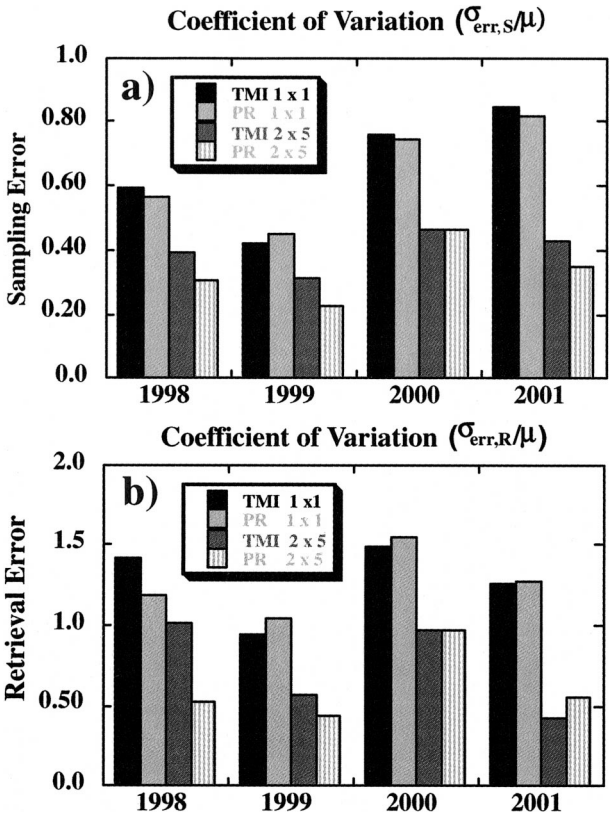

FIG. 8. Coefficients of variation computed at 1° × 1° and 2° × 5° scales comparing (a) sampling errors and (b) retrieval errors for both the TMI and PR. The coefficient of variation estimates the error as the ratio of standard error ($\sigma_{err,S}$, $\sigma_{err,R}$) relative to the mean (μ) for each sensor (see Tables 4 and 5).

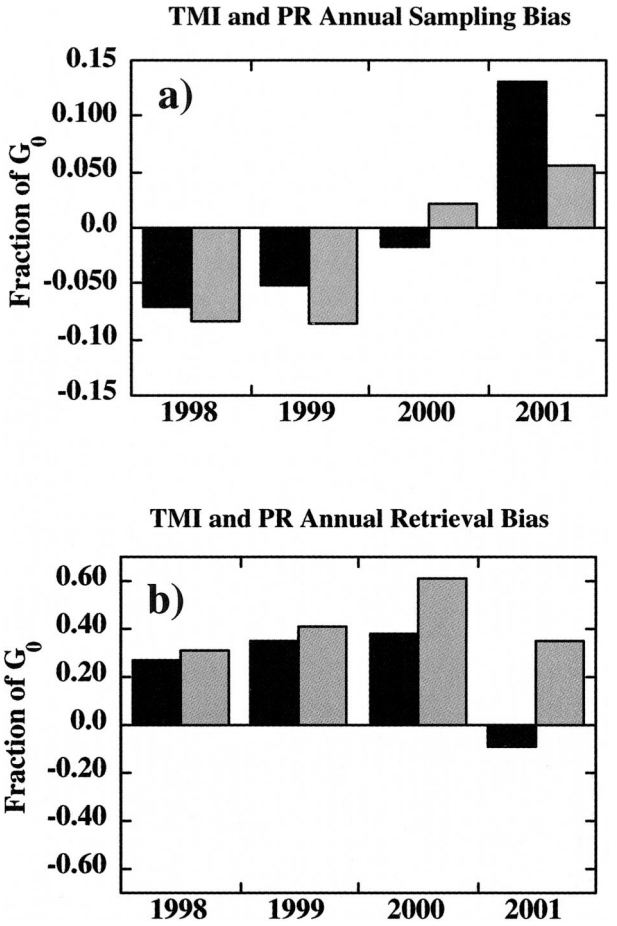

FIG. 9. Bar plot showing (a) sampling biases and (b) retrieval biases for the TMI (black) and the PR (gray) for each year of the study. Results shown as a fraction of G_0.

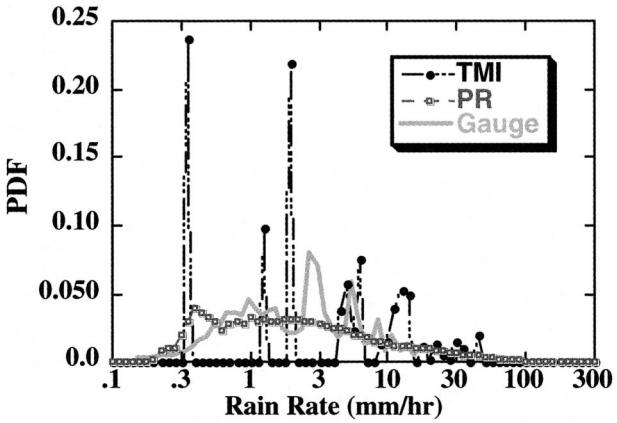

FIG. 10. Lognormal rain-rate distributions for the TMI, PR, and Oklahoma Mesonet gauges. TMI and PR profiles were constructed from 56 rain cases. Gauge profile was compiled from all data available over the 4 yr of study (1998–2001).

version 5 of the TMI ''land'' algorithm, the constraints of using only the 85-GHz brightness temperatures limits the database to 28 modeled cases, which can only support a discrete rain-rate distribution. This quantization in the rain-rate distribution is not observed in the TMI oceanic rain-rate profiles, which uses all nine channels. The TMI land algorithm is undergoing some improvements in the version-6 algorithm that will better distribute the algorithmically determined rain rates across a greater number of bins.

In contrast with the TMI, the PR distribution in Fig. 10 is more continuous and covers a larger dynamic range of observations, in general agreement with the climatological gauge distribution. Although the PR's distribution of instantaneous rain rates appeared to be more physically realistic, the TMI's retrieval biases were generally lower than the PR, demonstrating the importance of sampling and averaging in the climatological precipitation estimation.

The PR rain estimates are affected by three potential sources of retrieval error (Iguchi et al. 2000): 1) attenuation correction, 2) nonhomogenous beam filling of the PR footprint (i.e., presence of reflectivity gradients), and 3) stratiform–convective classification. With a transmitting frequency of 13.8 GHz, the PR is strongly attenuated by precipitation. The return power first undergoes an attenuation correction that produces an effective reflectivity factor Z_{eff}. In heavy-rain cases, this correction can change the estimated rain rate by an order of magnitude (Iguchi et al. 2000; Meneghini et al. 2000). Further corrections are applied to account for nonuniform beam filling associated with reflectivity gradients and each rainy pixel is assigned an assumed drop size distribution, using a dual *Z–R* stratiform–convective classification scheme.

Although it is difficult to observe in Fig. 10, the PR estimated more cases of high rain rates than the gauges. Close examination of convective cells in the 56 selected rain cases revealed correlated clusters of rain rates exceeding 200 mm h^{-1}, in cases that are typical of the rain regimes observed during the late spring and early summer months. These cases require a large attenuation correction and display strong reflectivity gradients. The *Z–R* relation itself has no upper limit and will generate very high rain rates for corresponding high *Z* values. Beam smearing may also be important for spreading higher-reflectivity values into adjacent bins (Iguchi et al. 2000). High-rain-rate cases have an especially large statistical impact on bulk monthly rain estimates, because the unconditional mean monthly rain rate depends on a relatively small number of observations.

c. Seasonal and diurnal precipitation climatology

Seasonal and diurnal variations over land at higher latitudes can also affect error statistics. In particular, it is important to understand how such variations affect retrievals and whether the TRMM rain algorithms are biased by cyclical climatological variability. This part of the study investigated the secondary effects of

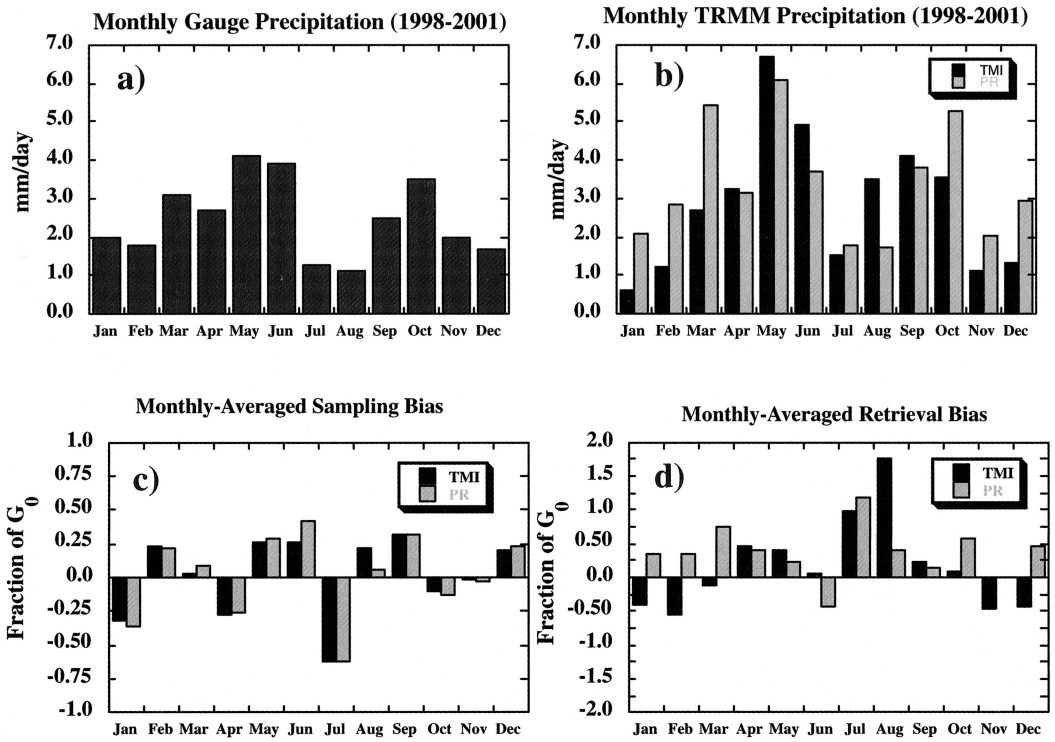

FIG. 11. Monthly accumulations for (a) the Oklahoma Mesonet rain gauges and (b) the TMI and PR averaged over all four study years at the 2° × 5° scale; (c) 4-yr monthly sampling and (d) retrieval biases for the TMI (black) and the PR (gray).

Oklahoma's seasonal and diurnal cycles on the TRMM sampling and retrievals at the 2° × 5° scale. Figure 11a displays a plot showing the 4-yr precipitation climatology for Oklahoma (1998–2001). The mean annual cycle, inferred by averaging all monthly accumulations from the 66 mesonet gauges used in the study, revealed a bimodal pattern in monthly precipitation amounts, with May and June showing the highest amount of precipitation and a second relative peak occurring in October. Monthly minima in precipitation are evident in July and February. Figure 11b shows a 4-yr monthly climatology for the TMI and PR. The TMI and PR revealed a similar annual precipitation cycle as the gauges, but in general tended to overestimate the monthly precipitation relative to the gauges. The PR recorded higher monthly precipitation accumulations than the TMI during the colder winter months, but the TMI estimates, interestingly, were higher relative to the PR during April, May, June, August, and September.

Figures 11c and 11d show the mean monthly sampling and retrieval biases for the TMI and PR as a fraction of G_0. These biases were averaged over all 4 yr of the study. In general, retrieval biases exceeded sampling biases by roughly a factor of 2. For both the TMI and the PR, the largest sampling biases ($\sim 0.60 G_0$) occurred in the month of July, a climatologically dry month, as shown in Fig. 11a. The July retrieval biases, on the other hand, were positive. This result seems to indicate that the two TRMM rain sensors were, on average, undersampling the precipitation during the month of July ($G_{\mathrm{TMI,PR}} - G_0 < 0$), while the rain algorithms were overestimating the observed precipitation during this month ($R_0 - G_{\mathrm{TMI,PR}} > 0$). August, however, which was also a relatively dry month, showed slightly positive sampling biases. One reason for this difference in the sampling biases could be attributed to a negative precipitation anomaly in 2000, during which most of the mesonet gauges recorded no precipitation for the month of August. Random errors could have also contributed to this result.

In the Midwestern plains, a large fraction of the precipitation occurs in association with convective rain systems, especially during the transition period between cold and warm seasons. TRMM sensors may be oversampling these rain systems. Significant sampling biases were observed in the months of May, June, and September ($b_S > 0.25\ G_0$). Retrieval biases were also generally positive during these months. The PR retrieval biases were positive for all months accept June. The negative PR retrieval bias observed in June did not support the observed trend, but could be partly attributed to undersampling, because both sensors showed large negative sampling biases during this month ($b_S < -0.50\ G_0$). In general, though, both TMI and PR algorithms tended to overestimate in months

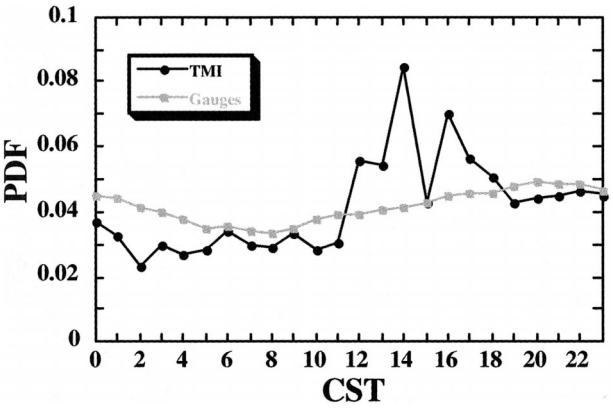

FIG. 12. PDF of diurnal precipitation accumulations for the TMI and the Oklahoma Mesonet gauges. Each hour represents the fractional contribution to the total diurnal precipitation. The time unit is central standard time (CST).

in which convective precipitation was most likely to occur.

One of the most interesting features in Fig. 11d was the negative TMI retrieval biases observed during the colder months of January, February, March, November, and December, versus the positive biases observed during the warmer months. McCollum et al. (2002) observed a similar pattern in the seasonal biases of the Goddard profiling algorithm (GPROF) estimates using Special Sensor Microwave Imager (SSM/I) data, suggesting a connection to the seasonal changes in the distribution of ice above the freezing level (e.g., particle size, shape, and number density). They related this observation to smaller ice-scattering cross sections associated with wintertime stratiform precipitation. The negative winter retrieval biases for the TMI also partly explain the observed differences in the overall annual retrieval biases between the two sensors.

Figure 12 shows the normalized diurnal precipitation profiles for the gauges and the TMI, plotting the hourly rain accumulations relative to the total diurnal precipitation. Hourly precipitation totals for the TMI were computed from the gridded Level-2 products. A similar profile could not be computed for the PR because gridded 2A25 data are not currently made available. An examination of Fig. 12 revealed the presence of a positive TMI bias in the afternoon (1200–1800 CST) relative to the gauges. The timing of this feature is reasonably well correlated with the production of ice particles typical of convective systems that form in the afternoon, an observation consistent with the results of Mohr and Zipser (1996), who classified mesoscale convective systems (MCSs) over land and ocean using the TMI 85-GHz channel, and showed the existence of strong correlations between the TMI hourly rain accumulations and the late afternoon development of MCSs over land, as indicated by the 85-GHz scattering signature.

7. Discussion of systematic effects of discrete sampling at high latitudes on TRMM rain estimates

TRMM sampling statistics are affected by the orbital characteristics of the satellite and by climatological cycles. The planning focus for the TRMM mission was on sampling over the equatorial oceans. However, while the TRMM sampling frequency in the Tropics is relatively constant, this is not true at high latitudes. Moreover, precipitation over the tropical oceans has a fairly modest diurnal cycle, whereas over midlatitude continental regions, such as Oklahoma, precipitation patterns are influenced by a number of climate patterns acting over a broad spectrum of time scales (e.g., diurnal, synoptic, annual).

Prior to the launch of TRMM, Laughlin (1981) and McConnell and North (1987) examined the sampling problem by analyzing data from GATE. These studies considered the sampling frequency to be constant and relied on rain statistics that were relatively insensitive to diurnal variations. Other studies, such as Shin and North (1988) and Bell et al. (1990) showed more clearly that variations in the sampling frequency at the higher latitudes directly affected the predicted sampling variance. These latter studies indicated that the uneven sampling frequency at the higher latitudes would increase sampling errors, although some of this error would be offset by the increasing sampling frequency near the turning latitude.

The most important time parameter to consider in this case is the autocorrelation time, which statistically corresponds to a time threshold when satellite overpasses can be treated as representing independent observations. As Laughlin (1981) clearly showed, this parameter varies with the size of the area being sampled. For cases in which the sampling interval is much less than the autocorrelation time, contiguous samples are dependent, reducing the effective number of total samples, whereas if the sampling frequency is much greater than the autocorrelation time, the sampling becomes less and less representative of the actual precipitation.

Because Oklahoma is located at the satellite's turning point, its sampling is bimodal, with sampling intervals 21.6 and 1.6 h related to the switchover between ascending and descending orbits. Averaged over the 4-yr study period, the mean revisit time is about 10.5 h. Although the total number of overpasses is determined by the mean satellite revisit time, the number of independent samples involves both the sampling frequency and the fraction of the area covered by the satellite's swath relative to the sampling domain (see Shin and North 1989 and Bell et al. 1990).

The autocorrelation time for the $2^\circ \times 5^\circ$ study area shown in Fig. 1 was earlier estimated to be about 8 h. By this measure, it becomes clear that TRMM sensors are either routinely undersampling or oversampling the region. When the sampling interval is equal to 21.6 h,

the precipitation across the region is undersampled. Laughlin (1981) showed that sampling errors increased by about a factor of 2 when the sampling interval was increased from 12 to 24 h.

The opposite situation occurs when the sampling interval is equal to 1.6 h, resulting in contiguous observations being too close together to be considered statistically independent. The situation becomes even more complicated when considering the complex interaction of the sampling process with precipitation variability at a number of different time scales. Considering these facts, it is not surprising that results of this study revealed higher random sampling errors than previous studies simulated under more ideal conditions.

8. Conclusions

This paper examined a validation strategy designed to estimate sampling and retrieval errors and biases for monthly TMI and PR precipitation estimates over a 2° × 5° region of Oklahoma. This region covered an area that closely matched the size of a standard TRMM grid box of 5° × 5°. The proposed error model estimated bulk climatological sampling and retrieval errors using a simple technique that subsampled a network of gauge data at TRMM overpass times. The subsampling of the rain gauge precipitation time series produced sensor-dependent rain estimates for the TMI and PR. These gauge-inferred estimates were subsequently assumed to include the temporal sampling errors associated with each sensor, and provided the additional information needed to decouple the sampling and retrieval errors for the two TRMM sensors.

The results of this analysis can be highlighted as follows:

- Overall, TMI random sampling and retrieval standard errors were less than the PR, but the PR showed a smaller coefficient of variation. The PR also showed a proportionately larger reduction in random errors when the analysis was extended from a 1° × 1° to a 2° × 5° scale.
- Statistical regressions showed evidence of a conditional sampling bias for the TMI that was characterized by an overestimation of precipitation for high-precipitation months and an underestimation for low-precipitation months. The PR, likewise, showed a positive conditional sampling bias for high-precipitation months, but its estimates appeared to be more consistent with gauge estimates for lower amounts.
- Bulk sampling and retrieval biases estimated relative to the gauge annual means G_0 tended to be higher for the PR than the TMI.
- A comparison of satellite and gauge instantaneous precipitation rates revealed a closer similarity between the PR and the gauge PDFs. The TMI version-5 rain-rate PDF, on the contrary, was discretely distributed because of the matching of TMI brightness temperatures to a database that only consisted of 28 modeled cases.
- An examination of monthly averaged retrieval biases for the TMI and PR displayed negative biases during the colder months versus positive biases during the warmer months. The retrieval biases inferred for the PR tended to be positive for all months.
- A comparison of the normalized TMI and gauge diurnal precipitation cycle revealed a positive TMI afternoon bias.
- Estimated sampling errors exceeded prelaunch predictions. It is suspected that this result was due to the uneven sampling intervals associated with TRMM sampling at the satellite's turning point, and precipitation variability associated with midlatitude climate cycles for the central United States. Both of these factors would tend to increase random sampling variance, which also appeared as a year-to-year sampling bias when averaged over an annual time scale.

The error model applied in this study can easily be applied to other regions, but, as this study shows, it is important to optimize the areal coverage and density of gauges to the standard satellite grid box. The estimated errors in gauge and satellite-inferred precipitation estimates suggest that 1° × 1° grid boxes are too small because of the time–space autocorrelation between the ground and satellite datasets. It will also be important in the future to test this methodology using rain estimates from ground-based radars, which provide estimates over a spatial continuum. Radars also collect observations of precipitation aloft, which, from a remote sensing standpoint, are more characteristically similar to the satellite.

Acknowledgments. I deeply thank Dr. George Huffman for his careful review of the final manuscript and all of his scientific expertise in the area of satellite–gauge validation. Our discussions over the last two years have been an invaluable source of knowledge in this research. I also thank Dr. Tom Bell for the informative conversations we have had on TRMM sampling.

REFERENCES

Adler, R. F., G. J. Huffman, and P. R. Keehn, 1994: Global tropical estimates from microwave-adjusted geosynchronous IR data. *Remote Sens. Rev.,* **11,** 125–152.

Barnston, A. G., 1991: An empirical method of estimating raingage and radar rainfall measurement bias and resolution. *J. Appl. Meteor.,* **30,** 282–296.

Bell, T. L., and P. K. Kundu, 2003: Comparing satellite rainfall estimates with rain-gauge data: Optimal strategies suggested by a spectral model. *J. Geophys. Res.,* **108,** 4121, doi:10.1029/2002JD002641.

——, A. Abdullah, R. L. Martin, and G. North, 1990: Sampling errors for satellite-derived tropical rainfall: Monte Carlo study using a space–time stochastic model. *J. Geophys. Res.,* **95,** 2195–2205.

——, P. K. Kundu, and C. D. Kummerow, 2001: Sampling errors of SSM/I and TRMM rainfall averages: Comparison with error es-

timates from surface data and a simple model. *J. Appl. Meteor.*, **40,** 938–954.
Brock, F. V., K. C. Crawford, R. L. Elliot, G. W. Cuperus, S. J. Stadler, H. J. Johnson, and M. D. Eilts, 1995: The Oklahoma Mesonet: A technical overview. *J. Atmos. Oceanic Technol.*, **12,** 5–18.
Chang, A. T. C., and L. Chiu, 1999: Nonsystematic errors of monthly oceanic rainfall derived from SSM/I. *Mon. Wea. Rev.*, **127,** 1630–1638.
Ferraro, R. R., and G. F. Marks, 1995: The development of SSM/I rain-rate retrieval algorithms using ground-based radar measurements. *J. Atmos. Oceanic Technol.*, **12,** 755–770.
Habib, E., W. F. Krajewski, and A. Kruger, 2001: Sampling errors of tipping-bucket rain gauge measurements. *J. Hydrol. Eng.*, **6,** 159–166.
Huff, F. A., 1970: Sampling errors in measurement of mean precipitation. *J. Appl. Meteor.*, **9,** 35–45.
Huffman, G. J., 1997: Estimates of root-mean-square random error for finite samples of estimated precipitation. *J. Appl. Meteor.*, **36,** 1191–1201.
Hulme, M., and M. New, 1997: Dependence of large-scale precipitation climatologies on temporal and spatial sampling. *J. Climate*, **10,** 1099–1113.
Iguchi, T., T. Kozu, R. Meneghini, J. Awaka, and K. Okamoto, 2000: Rain-profiling algorithm for the TRMM precipitation radar. *J. Appl. Meteor.*, **39,** 2038–2052.
Krajewski, W. F., G. J. Ciach, J. R. McCollum, and C. Bacotiu, 2000: Initial validation of the Global Precipitation Climatology Project monthly rainfall over the United States. *J. Appl. Meteor.*, **39,** 1071–1087.
Kummerow, C., W. Barnes, T. Kozu, J. Shiue, and J. Simpson, 1998: The Tropical Rainfall Measuring Mission (TRMM) sensor package. *J. Atmos. Oceanic Technol.*, **15,** 809–817.
——, and Coauthors, 2000: The status of the Tropical Rainfall Measuring Mission (TRMM) after two years in orbit. *J. Appl. Meteor.*, **39,** 1965–1982.
——, and Coauthors, 2001: The evolution of the Goddard Profiling Algorithm (GPROF) for rainfall estimation from passive microwave sensors. *J. Appl. Meteor.*, **40,** 1801–1820.
Laughlin, C. R., 1981: On the effect of temporal sampling on the observation of mean rainfall. Precipitation measurements from space. Workshop Report, NASA Publication, D59–D66.
McCollum, J. R., W. F. Krajewski, R. R. Ferraro, and M. B. Ba, 2002: Evaluation of biases of satellite rainfall estimation algorithms over the continental United States. *J. Appl. Meteor.*, **41,** 1065–1080.
McConnell, A., and G. North, 1987: Sampling errors in satellite estimates of tropical rain. *J. Geophys. Res.*, **92,** 9567–9570.
Meneghini, R., T. Iguchi, T. Kozu, L. Liao, K. Okamoto, J. A. Jones, and J. Kwiatkowski, 2000: Use of the surface reference technique for path attenuation estimates from the TRMM precipitation radar. *J. Appl. Meteor.*, **39,** 2053–2070.
Mohr, K. I., and E. Zipser, 1996: Mesoscale convective systems defined by their 85 GHz ice scattering signature: Size and intensity comparison over tropical oceans and continents. *Mon. Wea. Rev.*, **124,** 2417–2437.
Morrissey, M. L., and J. E., Janowiak, 1996: Sampling-induced conditional biases in satellite climate-scale rainfall estimates. *J. Appl. Meteor.*, **35,** 541–548.
——, J. A. Maliekal, J. S. Greene, and J. Wang, 1995: The uncertainty of simple spatial averages using rain gauge networks. *Water Resour. Res.*, **31,** 2011–2017.
North, G., and S. Nakamoto, 1989: Formalism for comparing rain estimation designs. *J. Atmos. Oceanic Technol.*, **6,** 985–992.
Rodriguez-Iturbe, I., and J. M. Mejia, 1974a: The design of rainfall networks in time and space. *Water Resour. Res.*, **10,** 713–728.
——, and ——, 1974b: On the transformation of point rainfall to areal rainfall. *Water Resour. Res.*, **10,** 729–735.
Serra, Y. L., and M. J. McPhaden, 2003: Multiple time- and space-scale comparisons of ATLAS buoy rain gauge measurements with TRMM satellite precipitation measurements. *J. Appl. Meteor.*, **42,** 1045–1059.
Shin, K., and G. R. North, 1988: Sampling error study for rainfall estimate by satellite using a stochastic model. *J. Appl. Meteor.*, **27,** 1218–1231.
——, ——, Y. Ahn, and P. A. Arkin, 1990: Time scales and variability of area-averaged tropical oceanic rainfall. *Mon. Wea. Rev.*, **118,** 1507–1516.
Simpson, J., R. F. Adler, and G. R. North, 1988: A proposed Tropical Rainfall Measuring Mission (TRMM) satellite. *Bull. Amer. Meteor. Soc.*, **69,** 278–294.
Spencer, R. W., H. M. Goodman, and R. E. Hood, 1989: Precipitation retrieval over land and ocean with the SSM/I: Identification and characteristics of the scattering signal. *J. Atmos. Oceanic Technol.*, **6,** 254–273.
Tao, W.-K., and J. Simpson, 1993: Goddard Cumulus Ensemble Model. Part I: Model description. *Terr. Atmos. Oceanic Sci.*, **4,** 35–72.
Wilheit, T. T., 1988: Error analysis for the Tropical Rainfall Measuring Mission (TRMM). *Tropical Rainfall Measurements*, J. S. Theon and N. Fugono, Eds., A. Deepak Publishing, 377–385.
Xie, P., and P. A., Arkin, 1995: An intercomparison of gauge observations and satellite estimates of monthly precipitation. *J. Appl. Meteor.*, **34,** 1143–1160.